arXiv:1606.06761v1 [cond-mat.mtrl-sci] 21 Jun 2016

# Interplay between spin-orbit coupling and crystal-field effect in topological insulators

Hyungjun Lee and Oleg V. Yazyev
*Institute of Theoretical Physics, Ecole Polytechnique Fédérale de Lausanne (EPFL), CH-1015 Lausanne, Switzerland*

(Dated: June 23, 2016)

Band inversion, one of the key signatures of time-reversal invariant topological insulators (TIs), arises mostly due to the spin-orbit (SO) coupling. Here, based on *ab initio* density-functional calculations, we report a theoretical investigation of the SO-driven band inversion in isostructural bismuth and antimony chalcogenide TIs from the viewpoint of its interplay with the crystal-field effect. We calculate the SO-induced energy shift of states in the top valence and bottom conduction manifolds and reproduce this behavior using a simple one-atom model adjusted to incorporate the crystal-field effect. The crystal-field splitting is shown to compete with the SO coupling, that is, stronger crystal-field splitting leads to weaker SO band shift. We further show how both these effects can be controlled by changing the chemical composition, whereas the crystal-field splitting can be tuned by means of uniaxial strain. These results provide a practical guidance to the rational design of novel TIs as well as to controlling the properties of existing materials.

PACS numbers: 71.20.Nr, 71.70.Ch, 71.70.Ej

## I. INTRODUCTION

Topology, originally one of the branches of mathematics, has been intimately linked to a variety of novel quantum phenomena in condensed matter physics[1,2]. One representative example is the integer quantum Hall effect (IQHE), which was observed in the two-dimensional (2D) electron gas in a strong magnetic field[3] and subsequently explained by using the topological structures of electron wave functions in momentum space[4]. More recently, topological notions have been invoked to clarify an exotic new quantum phase in time-reversal (TR) invariant band insulators, dubbed topological insulators (TIs)[5–9]. Unlike the IQHE, TIs preserve the TR symmetry and are topologically classified via the $\mathbb{Z}_2$ invariant[10–13]. As guaranteed by bulk-boundary correspondence, this bulk topological nature manifests itself in the robust spin-helical metallic boundary modes which are protected by the TR symmetry[5–9].

Nontrivial topology of TIs is accompanied by band inversion and TIs discovered to date theoretically or experimentally can be classified into *s*-*p*, *p*-*p*, and *d*-*f* types according to the orbital characters of states participating in band inversion[14,15]. The examples of TIs with *s*-*p* type band inversion include HgTe quantum wells[16], the first experimentally realized 2D TI (also called quantum spin Hall insulator)[17], as well as ternary semiconductors such as Heusler[18–20] and chalcopyrite compounds[21]. As an example, HgTe features the inverted band order, that is, the *s*-like $\Gamma_6$ state lies below the *p*-like $\Gamma_8$ states at the $\Gamma$ point[16]. The *p*-*p* type band inversion can be found in various compounds containing heavy *p*-block elements, notably Bi with the large atomic spin-orbit (SO) coupling constant of 1.25 eV for the valence 6*p* states[22]. These materials include $Bi_{1-x}Sb_x$ alloy[23], the first experimentally identified three-dimensional (3D) TI[24], the second confirmed 3D TIs of binary Bi chalcogenides ($Bi_2Se_3$ and $Bi_2Te_3$)[25–27], and their variants[28] such as $TlBiSe_2$[29,30], $PbBi_2Te_4$[31,32], and $Bi_2Te_2Se$ classes[33,34]. Among them, $Bi_2Se_3$ and $Bi_2Te_3$ along with $Sb_2Te_3$ commonly exhibit the band inversion at the $\Gamma$ point between two $p_z$-type states nearest to the Fermi energy ($E_F$) with opposite parities, thus leading to topologically nontrivial phase[25]. Lastly, the *d*-*f* type band inversion mostly appears in correlated materials such as actinide compounds[35] and mixed-valence compounds[36,37]; for instance, the band inversion in mixed-valence $SmB_6$ occurs between the $4f$ and $5d$ states, such that one $5d$ state moves below the $4f$ states at three $X$ points[36]. In the examples above, band inversion occurs mostly due to the SO coupling. For this reason, all discovered TIs have the high-$Z$ elements with the strong atomic SO coupling as their constituents. Materials involving heavy elements thus constitute natural candidates to host topologically nontrivial phases.

Typically, the SO interaction induces splitting in band structures in various ways by coupling the electron's spin and orbital degrees of freedom[38]. The SO-induced splitting in solids can be broadly divided into the following two classes according to the presence or absence of inversion symmetry: (1) in inversion-symmetric materials such as diamond-type semiconductors, the SO interaction produces the band splittings, giving rise to, for example, the SO gap and the heavy-hole-light-hole splitting near the valence-band edge[38]; (2) in inversion-asymmetric materials such as zinc-blende-type semiconductors and metallic surfaces, it results in the additional spin splittings, for example, the Dresselhaus[39] and Rashba-Bychkov[40] effects. In its extreme manifestation, the SO interaction leads to the nontrivial electronic topology in TIs through band inversion. In this sense, the SO coupling has been considered as the essential ingredient to realize the topological order in TIs by taking the role of magnetic field in IQHE[5–8]. Going one step further, as one of the possible routes to enhance bulk band gap in TIs[41,42], there has been recently considerable interest in the interplay of the SO coupling with other effects such as the electron-electron interaction[35,43].

In the present work, we investigate the interplay be-

tween the SO coupling and the crystal-field effect in TIs by using *ab initio* density-functional-theory calculations. For this purpose, we consider the prototypical 3D TIs, Bi and Sb chalcogenides, all of which are isostructural layered compounds, thus being the ideal playground for exploring the interplay between the SO coupling and the crystal-field effect. The SO-induced shifts of the valence and conduction bands are responsible for band inversion in the above-mentioned materials, which eventually results in the emergence of TI phase. We introduce a simple model based on one-atom system incorporating the crystal-field effect. This model clearly demonstrates that the magnitude of the SO-driven shift of the valence and conduction band states is intimately related to the crystal-field splitting of these states. Moreover, we show how both the SO coupling and the crystal-field effect can be controlled by changing the chemical composition, whereas the latter effect can be tuned separately by means of uniaxial strain. The results of our work provide a practical guidance to the rational design of novel TIs as well as to controlling the properties of existing materials.

The rest of the manuscript is organized as follows: In Sec. II, we describe our density-functional-theory computational methodology. Sec. III discusses the main results of our work. Namely, it introduces the simple atomic picture of the interplay between the SO coupling and the crystal-field effect, then discusses the first-principles calculations carried out on TIs of different chemical composition as well as the effects of uniaxial pressure. Sec. IV concludes our paper.

## II. COMPUTATIONAL METHODOLOGY

Our present calculations are based on first-principles density-functional-theory (DFT) methods[44,45] as implemented in the Quantum ESPRESSO (QE) package[46]. We employ the Perdew-Burke-Ernzerhof-type generalized gradient approximation for the exchange-correlation energy[47] and the norm-conserving pseudopotentials (PPs)[48] generated according to the scheme of Troullier and Martins[49] as implemented in the APE code[50]. Wave functions are expanded using plane waves with kinetic-energy cutoff of 45 Ryd for all compounds considered. The Brillouin zone (BZ) is sampled with 8×8×8 Monkhorst-Pack meshes of special $\vec{k}$ points[51]. All used parameters were carefully checked to ensure the convergence of total energies to 1 mRyd.

To treat the SO coupling, two methods are used separately, both of which rely on the fully-relativistic PPs[52]: (1) for electronic structure calculations, one-shot perturbative treatment of the SO coupling based on the Hybertsen and Louie (HL) approach[53] with the perturbed SO Hamiltonian constructed using the wave functions from the scalar-relativistic calculations as unperturbed wave functions; (2) for atomic structure optimization calculations, full and self-consistent incorporation of the SO coupling with two-component spinor wave functions as implemented in QE[54]. The SO-driven band shift was calculated perturbatively via the HL approach as it is ambiguous how to determine the reference between the energies without and with the SO coupling. Thus, this perturbative approach constitutes a valuable tool for addressing the role of SO coupling separately from other effects. In order to assess the error due to the non-self-consistency in the HL formalism, we calculated electronic band structures from both methods and found that within the energy window of 3 eV centered around the Fermi level their differences are less than 0.1 eV for Bi chalcogenides while they are on the order of meV for Sb chalcogenides. Both the fully self-consistent approach[55] and the HL method[56,57] have been successfully applied to studying the bismuth chalcogenide TIs. For structural optimizations, we adopted the full treatment of the SO coupling. We used the experimentally determined crystal structures for all examined materials[58,59] with the exception of $Sb_2Se_3$ for which we optimized the lattice constants and internal coordinates due to the lack of the crystallographic data for the rhombohedral phase. In order to address the effects of uniaxial pressure, we varied the lattice constant along the $c$ axis in the hexagonal unit cell and then fully relaxed the internal coordinates until the residual forces on all ions are less than 1 meV/Å.

## III. RESULTS

### A. Atomic picture

We start by considering the SO-induced energy splitting in the simplest configuration, a one-atom system with valence $p$ orbitals. It basically traces back to the fine-structure levels of the hydrogenic atom[60]. We choose a basis set of $\{|p_x,\uparrow\rangle, |p_x,\downarrow\rangle, |p_y,\uparrow\rangle, |p_y,\downarrow\rangle, |p_z,\uparrow\rangle, |p_z,\downarrow\rangle\}$, where $p_i$'s $(i = x, y, z)$ are the radial part of valence wave functions times the corresponding real spherical harmonics and $\uparrow$ ($\downarrow$) is the eigenstate of the $z$ component of the spin angular momentum operator. The total Hamiltonian with the SO interaction taken into account is then given by

$$H = \frac{\zeta}{2}\begin{pmatrix} 0 & 0 & -i & 0 & 0 & -1 \\ 0 & 0 & 0 & i & 1 & 0 \\ i & 0 & 0 & 0 & 0 & i \\ 0 & -i & 0 & 0 & i & 0 \\ 0 & 1 & 0 & -i & 0 & 0 \\ -1 & 0 & -i & 0 & 0 & 0 \end{pmatrix}, \qquad (1)$$

with $\zeta$ the atomic SO strength[61]. Here, we assume that before the SO interaction is introduced, all $p$-type orbitals have the same energy due to the central potential of nucleus (i.e., spherical symmetry) and the absence of spin polarization. The latter is not general and, typically, is not the case for isolated atoms with unpaired electrons[62]. However, this assumption is justified for

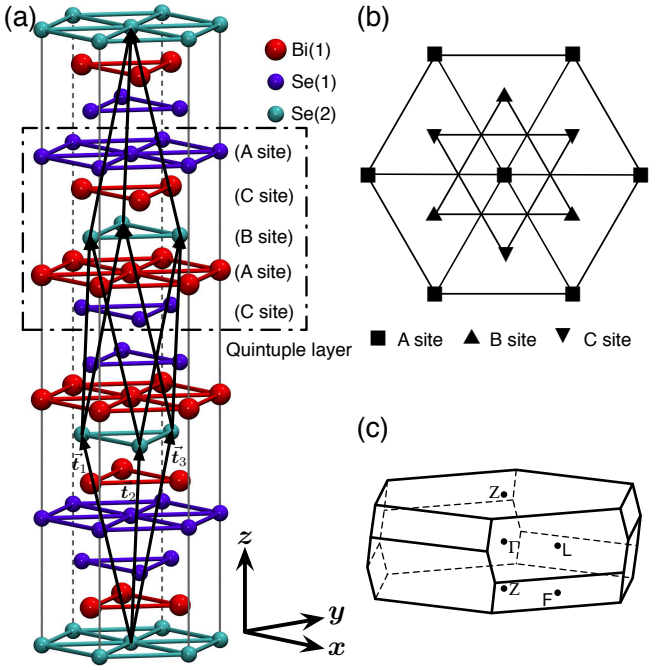


FIG. 1. (Color online) (a) Ball-and-stick representation of the bulk crystal structure of $Bi_2Se_3$ in which Bi atoms are indicated by red-colored balls and two inequivalent Se atoms by blue- (Se(1)) and cyan-colored (Se(2)) ones. A quintuple layer is marked by the dot-dashed rectangle with constituent atoms labeled according to the stacking sequence. Primitive lattice vectors $\vec{t}_i$ $(i = 1, 2, 3)$ are denoted with thick solid arrows and our chosen coordinate axes are also shown. (b) Top view along the (111) (trigonal) direction. Different triangular lattices are represented by rectangles, lower-, and upper-triangles. (c) First Brillouin zone (BZ) of $Bi_2Se_3$ bulk. Filled dots locate the high-symmetry $\vec{k}$ points that correspond to time-reversal invariant momenta.

the considered systems that are non-magnetic due to the combined effect of time-reversal and inversion symmetries similar to the case of Bi dimer[62]. This energy is set to 0 for simplicity. After diagonalizing this Hamiltonian, we obtain the following eigenenergies: $E_{j,m_j} = -\zeta$ (doublet) for $j = 1/2$ with $m_j = \pm 1/2$ and $\zeta/2$ (quadruplet) for $j = 3/2$ with $m_j = \pm 1/2$ and $\pm 3/2$, where $j$ is the total angular momentum and $m_j$ is its $z$ projection. For future reference, we list here the SO coupling parameters from experimental measurements[22] for the elements relevant to our study: $\zeta(\mathrm{Bi}) = 1.25\,\mathrm{eV}$, $\zeta(\mathrm{Te}) = 0.49\,\mathrm{eV}$, $\zeta(\mathrm{Sb}) = 0.40\,\mathrm{eV}$, and $\zeta(\mathrm{Se}) = 0.22\,\mathrm{eV}$.

Next, we examine the case with the lower symmetry in which the energies of $p$ orbitals without the SO coupling are differentiated from each other. This applies to the atoms in Bi and Sb chalcogenides crystallizing in the rhombohedral structure with the space group $R\bar{3}m$ (#166)[58,59]. With $Bi_2Se_3$ as an example, we show its bulk crystal structure in Fig. 1(a), the unit cell of which has five atoms, two Bi and three Se atoms with the Se atom labeled Se(2) as the inversion center. Of particular interest is its layered structure with a triangular lattice within each layer [Fig. 1(b)] and a quintuple layer (QL) as the building block which is stacked along the trigonal axis with a three-fold rotational symmetry[25,58]. We choose coordinate axes as follows: the $x$ axis is taken along the binary axis with the two-fold rotational symmetry, the $y$ axis is taken along the bisectrix axis, which is the intersection line of the reflection plane and atomic-layer plane, and the $z$ axis is along the trigonal axis perpendicular to the atomic layer.

Due to the layered crystal structure and the polarity of covalent bonds in these materials, the $p_x$ and $p_y$ orbitals are placed in different electrostatic environments compared with the $p_z$ orbital; both the positive ($E_{p_x} = E_{p_y} > E_{p_z}$) and negative ($E_{p_x} = E_{p_y} < E_{p_z}$) crystal-field splittings are realized[25,63]. The positive crystal-field splittings take place in the conduction-band states formed by the cation elements (Sb and Bi), while the negative crystal-field splittings of the valence-band states are shared by the anion elements (Se or Te). This behavior is common for all investigated binary materials as well as other Bi-based compounds such as BiTeI[64,65]. Below, we examine the cases of both positive and negative crystal-field splittings.

In order to incorporate the effects of positive crystal-field splitting ($E_{\mathrm{CF}} > 0$) typical for cation (Sb and Bi) sites, the total Hamiltonian should be modified in the following way:

$$H = \begin{pmatrix} E_{xy} & 0 & -i\zeta/2 & 0 & 0 & -\zeta/2 \\ 0 & E_{xy} & 0 & i\zeta/2 & \zeta/2 & 0 \\ i\zeta/2 & 0 & E_{xy} & 0 & 0 & i\zeta/2 \\ 0 & -i\zeta/2 & 0 & E_{xy} & i\zeta/2 & 0 \\ 0 & \zeta/2 & 0 & -i\zeta/2 & 0 & 0 \\ -\zeta/2 & 0 & -i\zeta/2 & 0 & 0 & 0 \end{pmatrix}, \quad (2)$$

where $E_{xy}$ represents the energy of the $p_x$ ($p_y$) orbitals without the SO coupling and that of $p_z$ orbitals without the SO coupling is fixed to 0 for convenience, thereby equating the crystal-field splitting $E_{\mathrm{CF}}$ to $E_{xy}$. By diagonalizing this Hamiltonian matrix, we can obtain the SO-induced energy splitting as a function of $E_{\mathrm{CF}}$ (all doublets):

$$E_{j,m_j} = \begin{cases} \frac{1}{4}\left(-\zeta + 2E_{\mathrm{CF}} - \sqrt{9\zeta^2 - 4\zeta E_{\mathrm{CF}} + 4E_{\mathrm{CF}}^2}\right) \\ \qquad\qquad \text{for } j = 1/2 \text{ and } |m_j| = 1/2 \\ \frac{1}{4}\left(-\zeta + 2E_{\mathrm{CF}} + \sqrt{9\zeta^2 - 4\zeta E_{\mathrm{CF}} + 4E_{\mathrm{CF}}^2}\right) \\ \qquad\qquad \text{for } j = 3/2 \text{ and } |m_j| = 1/2 \\ \frac{1}{2}\left(\zeta + 2E_{\mathrm{CF}}\right) \quad \text{for } j = 3/2 \text{ and } |m_j| = 3/2 \end{cases}. \quad (3)$$

Note that both $j$ and $m_j$ are not good quantum numbers for this Hamiltonian with non-zero crystal-field splitting, but we use the effective $j$ and $m_j$ for classification purposes. We also note that in the limiting case, $E_{\mathrm{CF}} \to \infty$, the energy of $j = 1/2$ states shifts downward due to the SO coupling by $\zeta/4$, i.e., one fourth of its maximum shift at zero crystal-field splitting.

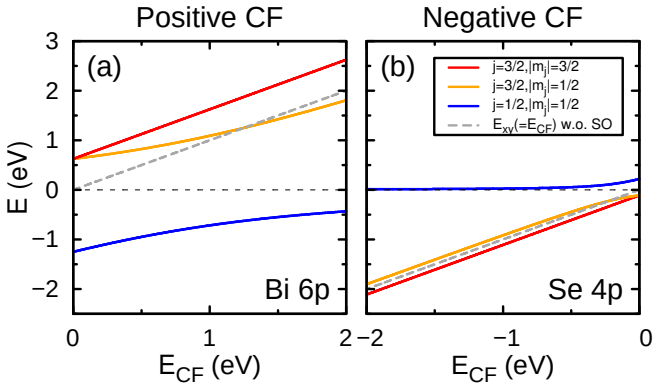


FIG. 2. (Color online) Atomic energy levels as a function of crystal-field splitting $E_{\rm CF}$ for (a) Bi $6p$ states and (b) Se $4p$ states at experimentally determined SO parameter values. As described in the main text, the positive and negative values of the crystal-field splitting are considered for Bi and Se atoms, respectively. All energy levels are labeled by the effective total angular momentum ($j$) and its $z$ component ($m_j$). Gray-dashed lines represent the energies of $p_x$ ($p_y$) orbitals ($E_{\rm xy}$) with those of $p_z$ ones fixed to 0 in absence of the SO coupling. Thin dashed lines indicate zero energy.

The negative crystal-field splitting scenario ($E_{\rm CF} < 0$) typical for the anion sites (Se and Te) is incorporated phenomenologically into the one-atom model by changing the sign of $\zeta$ in Eq. (2). It suffices for our purposes because we are interested mainly in the shift of $p_z$-like ($j = 1/2$) states closest to $E_{\rm F}$ rather than the details in entire $p$ manifold. The resulting eigenenergies are as follows:

$$E_{j,m_j} = \begin{cases} \frac{1}{4}\left(-\zeta + 2E_{\rm CF} + \sqrt{9\zeta^2 - 4\zeta E_{\rm CF} + 4E_{\rm CF}^2}\right) \\ \qquad\qquad \text{for } j = 1/2 \text{ and } |m_j| = 1/2 \\ \frac{1}{4}\left(-\zeta + 2E_{\rm CF} - \sqrt{9\zeta^2 - 4\zeta E_{\rm CF} + 4E_{\rm CF}^2}\right) \\ \qquad\qquad \text{for } j = 3/2 \text{ and } |m_j| = 1/2 \\ \frac{1}{2}\left(\zeta + 2E_{\rm CF}\right) \quad \text{for } j = 3/2 \text{ and } |m_j| = 3/2 \end{cases} . \tag{4}$$

Figures 2(a) and 2(b) show the eigenvalues of Hamiltonian (2) as a function of $E_{\rm CF}$ for the experimentally determined values[22] of SO parameter $\zeta$ of Bi $6p$ and Se $4p$ atomic states, respectively. In these figures, we focus only on positive values of $E_{\rm CF}$ for the Bi $6p$ states and on negative values of $E_{\rm CF}$ for the Se $4p$ states. From these figures, one can clearly see that the SO-driven splittings strongly depend on $E_{\rm CF}$. For Bi atom [Fig. 2(a)], the SO coupling first induces the splitting between $j = 1/2$ doublet and $j = 3/2$ quadruplet when $E_{\rm CF}$ is zero, then quadruplet splits further into two doublets, each with $|m_j| = 1/2$ and $3/2$ as $E_{\rm CF}$ increases. More precisely, at zero crystal-field splitting the $j = 1/2$ doublet is shifted downward by its maximum magnitude of 1.25 eV, then this magnitude decreases as $E_{\rm CF}$ increases, reaching about 0.43 eV when $E_{\rm CF}$ becomes 2 eV. In comparison to Bi atom with the positive crystal-field splitting, there are two distinct features in Se atom with the negative crystal-field splitting [Fig. 2(b)]: one is the reversal of the order of energy levels to arrange them from the lower energy in the following sequence, $E_{j=3/2,|m_j|=3/2}$, $E_{j=3/2,|m_j|=1/2}$, and $E_{j=1/2,|m_j|=1/2}$; the other is the opposite sign of the shift of the states. As compared to Bi atom, the $j = 1/2$ doublet of Se atom is shifted upward by its maximum magnitude of 0.22 eV at zero crystal-field splitting, whereas the $j = 3/2$ states are shifted downward. These results clearly show that depending on both the magnitude and the sign of the crystal-field splitting, the SO-driven splitting changes correspondingly and in particular, the maximum shift of the $j = 1/2$ doublet always occurs at zero crystal-field splitting. Hence, the relative importance of the SO coupling tends to diminish with the increase of the crystal-field splitting. We emphasize that in the case of discussed materials the $j = 1/2$ states of both cation and anion atoms are relevant to the top valence band and bottom conduction band states that exchange their order upon band inversion.

### B. Realistic materials

Keeping in mind the above results for SO-induced splitting in one-atom model system, we shall now turn our attention to the SO-driven band inversion in bismuth ($Bi_2Se_3$, $Bi_2SeTe_2$, and $Bi_2Te_3$) and antimony chalcogenides ($Sb_2Se_3$, $Sb_2SeTe_2$, and $Sb_2Te_3$). Except for $Sb_2Se_3$ with the orthorhombic phase (space group $Pbnm$) at ambient conditions[66], all these materials crystallize in the rhombohedral phase (space group $R\bar{3}m$)[58,59]. For comparison purposes, we assume the rhombohedral phase also for $Sb_2Se_3$.

Figure 3 shows the electronic band structures of bulk $Bi_2Se_3$ near the valence- and conduction-band edges around the $\Gamma$ point without and with the SO coupling, whose main features are common also in the band structures of other members of this class. As indicated in this figure, the wave functions at the $\Gamma$ point can be classified according to the irreducible representation of the space group $R\bar{3}m$[63]. In this layered crystal structure, as considered above for one-atom system, the in-plane orbitals ($p_x$ and $p_y$) are differentiated from the out-of-plane orbital ($p_z$), thus resulting in the crystal-field splitting between the $p_x$ ($p_y$)-dominated band with $\Gamma_3^+$ symmetry and the $p_z$-dominated one with $\Gamma_1^+$ or $\Gamma_2^+$ symmetry even before the SO coupling is considered[25,63]. The SO coupling further splits these band levels into three doublets, each of which belongs to the states of $|j = 1/2, |m_j| = 1/2\rangle$, $|j = 3/2, |m_j| = 1/2\rangle$, and $|j = 3/2, |m_j| = 3/2\rangle$[25,63]. Most importantly, at the $\Gamma$ point, the SO coupling reverses the band ordering between the top valence ($\Gamma_2^-$) and bottom conduction ($\Gamma_1^+$) bands with opposite parities, thereby realizing topologically nontrivial phase[25,67].

The strength of the SO coupling and the crystal-field effect in this class of materials may be different depending

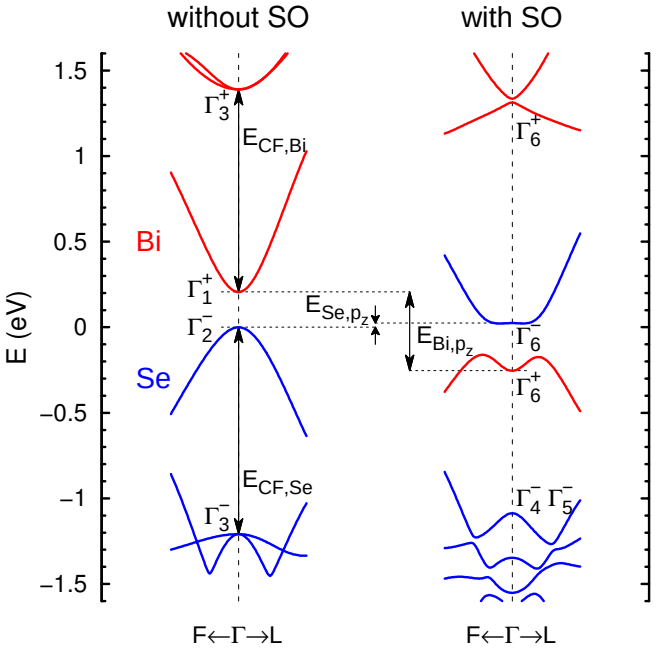


FIG. 3. (Color online) Band structures of bulk $Bi_2Se_3$ along the F-Γ-L path near the Γ point without and with the SO interaction. The energy of the valence band maximum at Γ without SO is set to 0. The energy bands are calculated along the path from Γ towards both F and L points up to the distance of 0.2 $Å^{-1}$, and are depicted with different colors according to the dominant atomic character at Γ. The states at Γ are labeled by the irreducible symmetry representation with the superscripts denoting the corresponding parity. The definitions of relevant energies discussed in the text are indicated by the arrows.

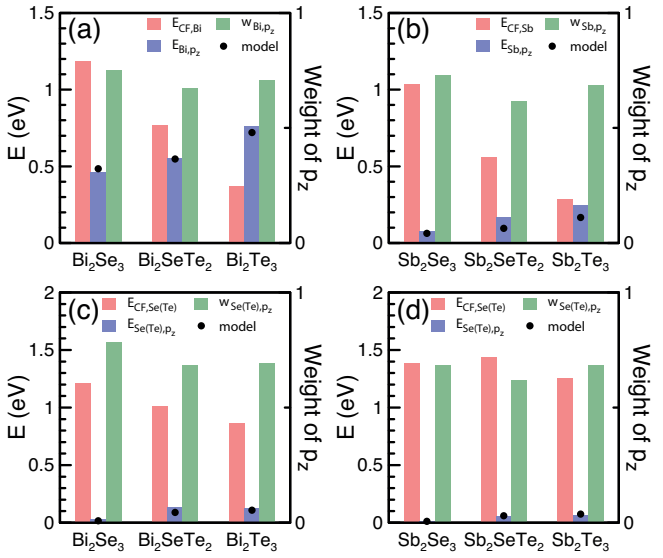


FIG. 4. (Color online) Bar diagrams revealing the effects of crystal field on SO-driven band shifts along a series of (a,c) Bi chalcogenides and (b,d) Sb chalcogenides. The depicted quantities are the crystal-field splittings, $E_{CF,Bi(Sb)}$ or $E_{CF,Se(Te)}$, of the conduction- or valence-band edges, the weight of $p_z$ orbital, $w_{Bi(Sb),p_z}$ ($w_{Se(Te),p_z}$), of cation (anion) atom in the bottom conduction (top valence) band at Γ without the SO coupling, and the magnitude of its SO-induced shift, $E_{Bi(Sb),p_z}$ and $E_{Se(Te),p_z}$, in presence of the SO coupling. Filled dots indicate the SO-driven shifts calculated using the one-atom model introduced in Sec. III A.

on distinct combinations of the anion and cation atomic species. The former is inherited from the atomic SO coupling while the latter depends on the coordination environments of constituent atoms and their relative electronegativities. As explained above, the SO-driven band shifts result from the interplay between these two factors. In order to verify this, for different combinations of elements we obtain at the Γ point the crystal-field splitting, $E_{CF,Bi(Sb)}$ or $E_{CF,Se(Te)}$, in cation (Bi, Sb)- or anion (Se, Te)-derived conduction- or valence-band edge and the weight, $w_{Bi(Sb),p_z}$ ($w_{Se(Te),p_z}$), of cation (anion) $p_z$ orbital in bottom conduction (top valence) state before the SO coupling is introduced; we then calculate perturbatively the shift of these $p_z$-type levels, $E_{Bi(Sb),p_z}$ and $E_{Se(Te),p_z}$, at the Γ point after the SO coupling is included. These results are shown for Bi and Sb chalcogenides in Figs. 4(a,c) and 4(b,d), respectively.

The substitution of Te for Se in Bi chalcogenides decreases the crystal-field splitting, likely because of the smaller electronegativity difference between Bi and Te compared to the Bi-Se pair. In Bi-derived conduction-band edge such substitution increases the shift of Bi $p_z$-type lowest conduction level ($E_{Bi,p_z}$) when the SO coupling is included [Fig. 4(a)]. More precisely, for Bi chalcogenides, the substitution of Te for Se decreases the crystal-field splitting, $E_{CF,Bi}$ and $E_{CF,Se(Te)}$, from 1.18 to 0.37 eV and from 1.21 to 0.86 eV in the bottom conduction and the top valence manifolds, respectively. In turn, owing to these changes of the crystal-field splitting, the SO-driven shifts, $E_{Bi,p_z}$ and $E_{Se(Te),p_z}$, of Bi $p_z$ and Se (Te) $p_z$ states increase from 0.46 to 0.76 eV and from 0.02 to 0.13 eV, respectively, both with the highest values in $Bi_2Te_3$. On the other hand, during these substitutions, the weights of Bi $p_z$ and Se (Te) $p_z$ states, $w_{Bi,p_z}$ and $w_{Se(Te),p_z}$, change little in bottom conduction and top valence states, respectively, and do not show any systematic tendency. The results for Sb chalcogenides in Figs. 4(b) and 4(d) show the same qualitative trends. However, due to the factor of 3 smaller atomic SO strength in Sb, the shift of Sb $p_z$-type level, $E_{Sb,p_z}$, in Sb chalcogenides is much smaller than $E_{Bi,p_z}$ in Bi chalcogenides.

Now, we briefly digress to recall the results obtained using the simple one-atom model. This model is expected to provide reasonable estimates of SO-driven splitting because the SO coupling is much more prominent deep in the core region, thus it can be safely approximated using the $\vec{k}$-independent term of the SO coupling in the $\vec{k} \cdot \vec{p}$ approximation analogous to the atomic SO coupling form[68]. In order to verify this argument we estimate the SO-driven shifts of Bi and Sb $p_z$-type levels nearest the Fermi level from the corresponding one-atom

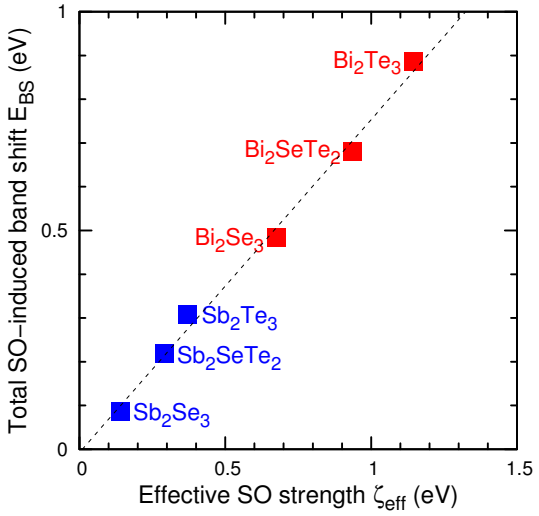


FIG. 5. (Color online) Relation between the effective spin-orbit strength $\zeta_{\rm eff}$ and the total SO-induced band shift $E_{\rm BS}$ in Bi and Sb chalcogenides. Dashed line is a fit to the data.

results, and compare these values with those obtained above. In this estimation, the SO-driven shift in real materials is obtained by multiplying the SO-induced shift of the $p_z$-dominant level ($j = 1/2$ doublet) from one-atom model by the weight of $p_z$ character of the corresponding atom in bottom conduction or top valence state at the $\Gamma$ point from DFT results for real materials without the SO coupling. For instance, the estimated SO-driven band shift $\tilde{E}_{{\rm Bi},p_z}$ of Bi $p_z$-like state in Bi chalcogenides is calculated by using the following expression: $\tilde{E}_{{\rm Bi},p_z} = |E_{{\rm Bi};j=1/2,|m_j|=1/2}| \times w_{{\rm Bi},p_z}$. As illustrated in Fig. 4, even though we used the minimal model based on one-atom system, the obtained results are consistent with those calculated using DFT with the SO interaction included using the HL method. The maximum deviation of 0.08 eV is observed for $Sb_2Te_3$. This rather large deviation can be ascribed to the relative large contribution of Te (31%), with its $\zeta$ similar to that of Sb, to the bottom conduction band without the SO coupling.

Relying on the existence of intimate relation between the SO-driven splitting and the crystal-field splitting, we can introduce an effective parameter which can be useful for assessing the SO-driven band shift in solids much as the atomic SO strength $\zeta$ does in atomic systems. Since there exists an inverse relation between the SO-induced band shift and the crystal-field splitting relevant to this band, we propose the following definition for the effective SO strength

$$\zeta_{\rm eff} = \sum_i \frac{\zeta_i}{1 + \frac{E_{{\rm CF},i}}{\zeta_i}}, \qquad (5)$$

where $i$ refers to the atomic species index, $\zeta_i$ is the atomic SO strength for the atom of species $i$, and $E_{{\rm CF},i}$ is the crystal-field splitting relevant to the bands dominated by this atom near $E_{\rm F}$. Then, we calculate the total SO-induced shift of the top valence and bottom conduction band states relative to each other $E_{\rm BS}$, e.g. for $Bi_2Se_3$, as $E_{\rm BS} = E_{{\rm Bi},p_z} + E_{{\rm Se},p_z}$.

Figure 5 shows $E_{\rm BS}$ as a function of $\zeta_{\rm eff}$ for Bi and Sb chalcogenides. Nearly linear relation between these two quantities is clearly visible in this figure. One can also see that the atomic SO strength is not fully utilized in solids and this degree of utilization is determined by the relevant crystal-field splitting. In this context, we note that our proposed effective SO strength can be used in solids as one of the alternatives instead of $\zeta$.

### C. Effect of uniaxial strain on band inversion

Finally, we consider the effect of strain on band inversion in the context of its intermediate role between the SO coupling and the crystal-field effect. Compressive or tensile strain, indeed, has been considered as one of the methods to realize the topological phase transition through band inversion[18,65,69,70]; the crystal-field splitting can also be tuned by applying pressure to materials[65]. In this regard, we examine, according to the applied uniaxial strain, the evolution of the band gap ($E_\Gamma$), the crystal-field splitting in conduction-band edge, the weight of Bi- or Sb-$p_z$ character in Bi or Sb $p_z$-like state nearest $E_{\rm F}$ at $\Gamma$ without SO, its SO-driven band shift, and the SO-induced band gap ($E_{\Gamma,{\rm SO}}$) at $\Gamma$. These results are shown in Fig. 6 for Bi chalcogenides ($Bi_2Se_3$ and $Bi_2Te_3$) and Sb chalcogenides ($Sb_2Se_3$ and $Sb_2Te_3$). In all cases, we apply uniaxial pressure along the (111) direction, the $z$ direction in our chosen coordinate system. For this purpose, we first vary the $z$ component of lattice vector ($c$) in the hexagonal cell from 95 % to 105 % with respect to its equilibrium value ($c_0$) and then optimize the internal atomic coordinates until the residual forces on all ions are less than 1 meV/Å.

As shown in Fig. 6, for all considered materials strain clearly changes the crystal-field splitting: for compressive strain, the crystal-field splitting decreases, while for tensile strain, it increases. This dependence can be rationalized from the following standpoint: compressive strain increases the local symmetry of coordination spheres of atoms in highly anisotropic layered materials. The change of crystal-field splitting upon varying strain is rather small, which in turn induces a relatively small change of SO-driven band shift. For instance, in $Bi_2Se_3$ [Fig. 6(a)], the crystal-field splitting in Bi-dominant bottom conduction manifold without SO ($E_{\rm CF,Bi}$) gradually increases from 1.05 to 1.19 eV as strain changes $c/c_0$ from 0.95 to 1.05. Under this rather small change in $E_{\rm CF,Bi}$, the SO-driven shift of Bi $p_z$-like state closest to $E_{\rm F}$ ($E_{{\rm Bi},p_z}$) varies inversely proportional to $E_{\rm CF,Bi}$ from 0.45 to 0.55 eV. As compared to $Bi_2Se_3$, the much smaller crystal-field splitting in $Bi_2Te_3$ gives rise to the larger SO-driven shift of Bi $p_z$-type level than in $Bi_2Se_3$ ranging from 0.71 to 0.83 eV [Fig. 6(b)]. For Sb chalcogenides [Figs. 6(c) and 6(d)], within the whole pressure

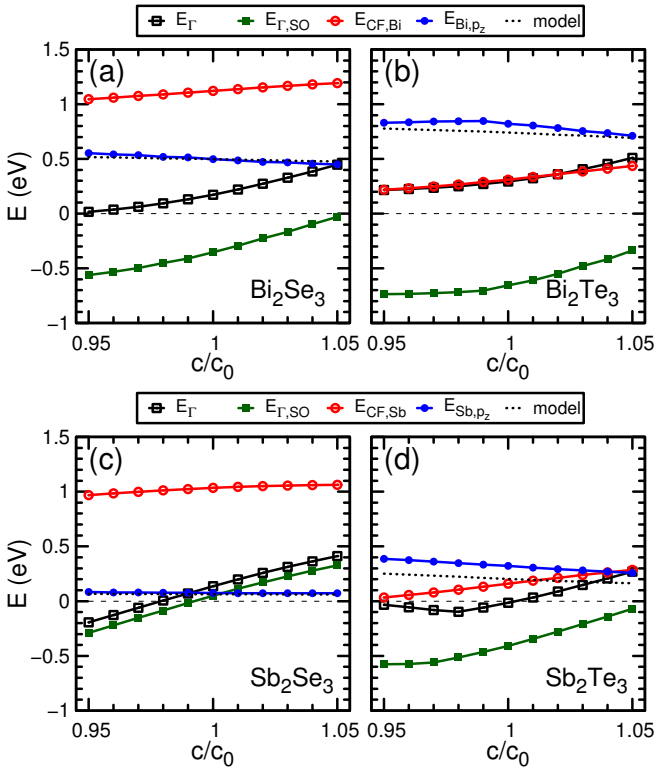


FIG. 6. (Color online) Effect of uniaxial strain on band inversion in (a,b) Bi chalcogenides and (c,d) Sb chalcogenides. The evolution of the band gap ($E_\Gamma$) and the crystal-field splitting ($E_{\mathrm{CF,Bi}}$ and $E_{\mathrm{CF,Sb}}$) in the bottom conduction manifold at Γ without SO is shown as a function of uniaxial strain along the $z$ axis. We also show the evolution of the SO-driven band shift ($E_{\mathrm{Bi},p_z}$ or $E_{\mathrm{Sb},p_z}$) of Bi or Sb $p_z$-like state closest to $E_\mathrm{F}$ and the SO-induced band gap ($E_{\Gamma,\mathrm{SO}}$) at Γ. The SO-driven shift calculated using the one-atom model is indicated with dotted lines.

range investigated, the smaller $\zeta$ in Sb atom results in the smaller SO-induced band shift of Sb $p_z$-like state closest to $E_\mathrm{F}$ than that in the corresponding Bi chalcogenides. We also notice that the model based on the one-atomic picture can explain semi-quantitatively this evolution of SO-driven shift of Bi or Sb $p_z$-type level as well, with the maximum deviation of about 0.14 eV in $Sb_2Te_3$ from the result obtained via DFT plus HL methods. This maximum deviation can also be explained by the non-negligible weight of Te in Sb $p_z$-like state.

In contrast to small change in the crystal-field splitting, the band gap changes significantly over the considered pressure range even before the SO coupling is included. Hence, we can see that the pressure-driven energy shift is of as much importance to the topological quantum phase transition through band inversion as the SO effect. This prominent role of the pressure-induced energy shift can be explained by the opposite shift of the energies of cation $p_z$ bonding and anion $p_z$ antibonding states near $E_\mathrm{F}$ upon compression or expansion[71]. In fact, both the inter-QL distance and the interlayer distance within a QL decrease as $c/c_0$ decreases, thereby leading to, e.g. for $Bi_2Se_3$, the opposite shift of the Bi $p_z$-like bonding and Se $p_z$-like antibonding states irrespective of the SO coupling[71]. This reduction of layer distance has a comparatively small influence on the SO-induced band shift since the SO coupling is substantially strong near the core region of the atom.

As far as the topological phase transition is concerned, all investigated materials except for $Sb_2Se_3$ show the topologically nontrivial phase throughout the considered pressure range. For $Sb_2Se_3$, the topological phase transition takes place at a compressive strain of $c/c_0 = 0.99$. This critical point is consistent with that in the previous literature[72]. As a final note, the upshift of $E_\Gamma$ below the point of $c/c_0 = 0.98$ in Fig. 6(d) for $Sb_2Te_3$ is attributed to the change of band ordering near the valence-band edge between Te $p_x$ ($p_y$)-like and Sb $p_z$-like states.

## IV. CONCLUSION

In summary, we investigated the SO-driven band inversion in TIs from the viewpoint of its interplay with the crystal-field effect, based on *ab initio* density-functional calculations. We calculated perturbatively the SO-induced energy shift of states near the Fermi level and demonstrated that this shift depends on the crystal-field splitting. This behavior is semi-quantitatively reproduced by the simple model based on the one-atom system adjusted to incorporate the crystal-field effect. The crystal-field splitting is shown to compete with the SO coupling, that is, stronger crystal-field splitting leads to weaker SO band shift. We further demonstrated how both these effects can be controlled by changing the chemical composition, whereas the crystal-field splitting can be tuned by means of uniaxial strain. Our results provide a helpful guideline for the discovery of novel materials realizing topologically nontrivial phases, or for tuning the properties of known topological insulators.

## ACKNOWLEDGMENTS

We were supported by the Swiss NSF (Grant No. PP00P2_133552) and the European Research Council starting grant "TopoMat" (Grant No. 306504). First-principles computations have been performed at the Swiss National Supercomputing Centre under Project Nos. s443 and s515.

[1] M. I. Monastyrsky, ed., *Topology in Condensed Matter*, Springer Series in Solid-State Sciences, Vol. 150 (Springer, Berlin, 2006).

[2] A. Altland and B. Simons, *Condensed Matter Field Theory*, 2nd ed. (Cambridge University Press, Cambridge, England, 2010).
[3] K. von Klitzing, G. Dorda, and M. Pepper, Phys. Rev. Lett. **45**, 494 (1980).
[4] D. J. Thouless, M. Kohmoto, M. P. Nightingale, and M. den Nijs, Phys. Rev. Lett. **49**, 405 (1982).
[5] M. Z. Hasan and C. L. Kane, Rev. Mod. Phys. **82**, 3045 (2010).
[6] X.-L. Qi and S.-C. Zhang, Rev. Mod. Phys. **83**, 1057 (2011).
[7] J. E. Moore, Nature **464**, 194 (2010).
[8] B. A. Bernevig and T. L. Hughes, *Topological Insulators and Topological Superconductors* (Princeton University Press, Princeton, NJ, 2013).
[9] Y. Ando, J. Phys. Soc. Jpn. **82**, 102001 (2013).
[10] C. L. Kane and E. J. Mele, Phys. Rev. Lett. **95**, 146802 (2005).
[11] J. E. Moore and L. Balents, Phys. Rev. B **75**, 121306 (2007).
[12] L. Fu, C. L. Kane, and E. J. Mele, Phys. Rev. Lett. **98**, 106803 (2007).
[13] R. Roy, Phys. Rev. B **79**, 195322 (2009).
[14] Z. Zhu, Y. Cheng, and U. Schwingenschlögl, Phys. Rev. B **85**, 235401 (2012).
[15] H. Zhang and S.-C. Zhang, Phys. Status Solidi RRL **7**, 72 (2013).
[16] B. A. Bernevig, T. L. Hughes, and S.-C. Zhang, Science **314**, 1757 (2006).
[17] M. König, S. Wiedmann, C. Brüne, A. Roth, H. Buhmann, L. W. Molenkamp, X.-L. Qi, and S.-C. Zhang, Science **318**, 766 (2007).
[18] S. Chadov, X. Qi, J. Kübler, G. H. Fecher, C. Felser, and S. C. Zhang, Nat. Mater. **9**, 541 (2010).
[19] H. Lin, L. A. Wray, Y. Xia, S. Xu, S. Jia, R. J. Cava, A. Bansil, and M. Z. Hasan, Nat. Mater. **9**, 546 (2010).
[20] D. Xiao, Y. Yao, W. Feng, J. Wen, W. Zhu, X.-Q. Chen, G. M. Stocks, and Z. Zhang, Phys. Rev. Lett. **105**, 096404 (2010).
[21] W. Feng, D. Xiao, J. Ding, and Y. Yao, Phys. Rev. Lett. **106**, 016402 (2011).
[22] K. Wittel and R. Manne, Theor. Chim. Acta **33**, 347 (1974).
[23] L. Fu and C. L. Kane, Phys. Rev. B **76**, 045302 (2007).
[24] D. Hsieh, D. Qian, L. Wray, Y. Xia, Y. S. Hor, R. J. Cava, and M. Z. Hasan, Nature **452**, 970 (2008).
[25] H. Zhang, C.-X. Liu, X.-L. Qi, X. Dai, Z. Fang, and S.-C. Zhang, Nat. Phys. **5**, 438 (2009).
[26] Y. Xia, D. Qian, D. Hsieh, L. Wray, A. Pal, H. Lin, A. Bansil, D. Grauer, Y. S. Hor, R. J. Cava, and M. Z. Hasan, Nat. Phys. **5**, 398 (2009).
[27] Y. L. Chen, J. G. Analytis, J.-H. Chu, Z. K. Liu, S.-K. Mo, X. L. Qi, H. J. Zhang, D. H. Lu, X. Dai, Z. Fang, S. C. Zhang, I. R. Fisher, Z. Hussain, and Z.-X. Shen, Science **325**, 178 (2009).
[28] B. Yan and S.-C. Zhang, Rep. Prog. Phys. **75**, 096501 (2012).
[29] H. Lin, R. S. Markiewicz, L. A. Wray, L. Fu, M. Z. Hasan, and A. Bansil, Phys. Rev. Lett. **105**, 036404 (2010).
[30] T. Sato, K. Segawa, H. Guo, K. Sugawara, S. Souma, T. Takahashi, and Y. Ando, Phys. Rev. Lett. **105**, 136802 (2010).
[31] T. Menshchikova, S. Eremeev, Y. Koroteev, V. Kuznetsov, and E. Chulkov, JETP Lett. **93**, 15 (2011).
[32] S. Souma, K. Eto, M. Nomura, K. Nakayama, T. Sato, T. Takahashi, K. Segawa, and Y. Ando, Phys. Rev. Lett. **108**, 116801 (2012).
[33] Z. Ren, A. A. Taskin, S. Sasaki, K. Segawa, and Y. Ando, Phys. Rev. B **82**, 241306 (2010).
[34] A. A. Taskin, Z. Ren, S. Sasaki, K. Segawa, and Y. Ando, Phys. Rev. Lett. **107**, 016801 (2011).
[35] X. Zhang, H. Zhang, J. Wang, C. Felser, and S.-C. Zhang, Science **335**, 1464 (2012).
[36] F. Lu, J. Zhao, H. Weng, Z. Fang, and X. Dai, Phys. Rev. Lett. **110**, 096401 (2013).
[37] X. Deng, K. Haule, and G. Kotliar, Phys. Rev. Lett. **111**, 176404 (2013).
[38] R. Winkler, *Spin-Orbit Coupling Effects in Two-Dimensional Electron and Hole Systems* (Springer-Verlag, Berlin, 2003).
[39] G. Dresselhaus, Phys. Rev. **100**, 580 (1955).
[40] Y. A. Bychkov and E. I. Rashba, JETP Lett. **39**, 78 (1984).
[41] M. Zhou, W. Ming, Z. Liu, Z. Wang, P. Li, and F. Liu, Proc. Nat. Acad. Sci. **111**, 14378 (2014).
[42] M. Zhou, W. Ming, Z. Liu, Z. Wang, Y. Yao, and F. Liu, Sci. Rep. **4**, 7102 (2014).
[43] D. Pesin and L. Balents, Nat. Phys. **6**, 376 (2010).
[44] P. Hohenberg and W. Kohn, Phys. Rev. **136**, 864 (1964).
[45] W. Kohn and L. J. Sham, Phys. Rev. **140**, A1133 (1965).
[46] P. Giannozzi, S. Baroni, N. Bonini, M. Calandra, R. Car, C. Cavazzoni, D. Ceresoli, G. L. Chiarotti, M. Cococcioni, I. Dabo, A. Dal Corso, S. de Gironcoli, S. Fabris, G. Fratesi, R. Gebauer, U. Gerstmann, C. Gougoussis, A. Kokalj, M. Lazzeri, L. Martin-Samos, N. Marzari, F. Mauri, R. Mazzarello, S. Paolini, A. Pasquarello, L. Paulatto, C. Sbraccia, S. Scandolo, G. Sclauzero, A. P. Seitsonen, A. Smogunov, P. Umari, and R. M. Wentzcovitch, J. Phys.: Condens. Matter **21**, 395502 (2009).
[47] J. P. Perdew, K. Burke, and M. Ernzerhof, Phys. Rev. Lett. **77**, 3865 (1996).
[48] D. R. Hamann, M. Schlüter, and C. Chiang, Phys. Rev. Lett. **43**, 1494 (1979).
[49] N. Troullier and J. L. Martins, Phys. Rev. B **43**, 1993 (1991).
[50] M. J. Oliveira and F. Nogueira, Comput. Phys. Comm. **178**, 524 (2008).
[51] H. J. Monkhorst and J. D. Pack, Phys. Rev. B **13**, 5188 (1976).
[52] L. Kleinman, Phys. Rev. B **21**, 2630 (1980).
[53] M. S. Hybertsen and S. G. Louie, Phys. Rev. B **34**, 2920 (1986).
[54] A. Dal Corso and A. Mosca Conte, Phys. Rev. B **71**, 115106 (2005).
[55] O. V. Yazyev, J. E. Moore, and S. G. Louie, Phys. Rev. Lett. **105**, 266806 (2010).
[56] E. Kioupakis, M. L. Tiago, and S. G. Louie, Phys. Rev. B **82**, 245203 (2010).
[57] O. V. Yazyev, E. Kioupakis, J. E. Moore, and S. G. Louie, Phys. Rev. B **85**, 161101 (2012).
[58] S. Nakajima, J. Phys. Chem. Solids **24**, 479 (1963).
[59] T. L. Anderson and H. B. Krause, Acta Crystallogr. B **30**, 1307 (1974).
[60] E. Condon and G. Shortley, *The Theory of Atomic Spectra* (Cambridge University Press, Cambridge, England, 1935).


[61] The atomic SO strength, $\zeta$, of an atomic orbital is

$$\zeta = \int \frac{\hbar^2}{2m_e^2c^2}\frac{1}{r}\frac{dV(r)}{dr}[R(r)]^2 r^2\, dr\,,$$

where $m_e$ is an electron mass, $V(r)$ is a potential, and $R(r)$ is the radial part of the atomic orbital.
[62] M. J. T. Oliveira and X. Gonze, J. Phys. B: At. Mol. Opt. Phys. **46**, 095101 (2013).
[63] C.-X. Liu, X.-L. Qi, H. Zhang, X. Dai, Z. Fang, and S.-C. Zhang, Phys. Rev. B **82**, 045122 (2010).
[64] M. S. Bahramy, R. Arita, and N. Nagaosa, Phys. Rev. B **84**, 041202 (2011).
[65] M. Bahramy, B.-J. Yang, R. Arita, and N. Nagaosa, Nat. Commun. **3**, 679 (2012).
[66] N. W. Tideswell, F. H. Kruse, and J. D. McCullough, Acta Crystallogr. **10**, 99 (1957).
[67] A. Pertsova and C. M. Canali, New J. Phys. **16**, 063022 (2014).
[68] E. O. Kane, J. Phys. Chem. Solids **8**, 38 (1959).
[69] B.-J. Yang and Y. B. Kim, Phys. Rev. B **82**, 085111 (2010).
[70] X. Xi, C. Ma, Z. Liu, Z. Chen, W. Ku, H. Berger, C. Martin, D. B. Tanner, and G. L. Carr, Phys. Rev. Lett. **111**, 155701 (2013).
[71] J. Liu, Y. Xu, J. Wu, B.-L. Gu, S. B. Zhang, and W. Duan, Acta Crystallogr. C **70**, 118 (2014).
[72] W. Liu, X. Peng, C. Tang, L. Sun, K. Zhang, and J. Zhong, Phys. Rev. B **84**, 245105 (2011).